Nanoscale

PAPER

View Article Online
View Journal | View Issue

Cite this: *Nanoscale*, 2017, **9**, 7235

Nonlinear photoluminescence in monolayer WS_2: parabolic emission and excitation fluence-dependent recombination dynamics†

Xiaopeng Fan,‡[a] Weihao Zheng,‡[a] Hongjun Liu,*[a] Xiujuan Zhuang,[a] Peng Fan,[a] Yanfang Gong,[a] Honglai Li,[a] Xueping Wu,[a] Ying Jiang,[a] Xiaoli Zhu,[a] Qinglin Zhang,[a] Hong Zhou,[a] Wei Hu,[a] Xiao Wang,[a] Xiangfeng Duan[b] and Anlian Pan*[a]

Received 23rd February 2017,
Accepted 23rd April 2017

DOI: 10.1039/c7nr01345k

rsc.li/nanoscale

Recombination dynamics during photoluminescence (PL) in two-dimensional (2D) semiconducting transition metal dichalcogenides (TMDs) are complicated and can be easily affected by the surroundings because of their atomically thin structures. Herein, we studied the excitation power and temperature dependence of the recombination dynamics on the chemical vapor deposition-grown monolayer WS_2 *via* a combination of Raman, PL, and time-resolved PL spectroscopies. We found a red shift and parabolic intensity increase in the PL emission of the monolayer WS_2 with the increasing excitation power and the decay time constants corresponding to the recombination of trions and excitons from transient PL dynamics. We attributed the abovementioned nonlinear changes in the PL peak positions and intensities to the combination of increasing carrier interaction and band structure renormalization rather than to the thermal effect from a laser. Furthermore, the excitation power-dependent Raman measurements support our conclusion. These findings and understanding will provide important information for the development of TMD-based optoelectronics and photonics.

Introduction

Transition metal dichalcogenides (TMDs), semiconducting layered materials with the common formula MX_2 (M = Mo and W; X = S, Se, and Te), have recently attracted significant interest due to their extraordinary electronic and optoelectronic properties.[1–11] Monolayer TMDs show great improvement in photoluminescence (PL) compared to bulk TMDs owing to the absence of interlayer perturbation and indirect to direct bandgap transition.[4–6,12–14] Due to the two-dimensional (2D) spatial confinement of electron motion and reduced Coulomb screening, strong many-body interactions, such as giant excitonic effects in these 2D TMDs systems, among carriers have been theoretically and experimentally reported.[14–23] On the other hand, because of their atomic thickness, the PL peak position and emission intensity for TMDs were found to be greatly affected by the surroundings such as the collected positions,[24,25] the density of defects,[26,27] and temperatures.[28,29] Both the abovementioned effects, the giant excitonic effects and the sensitivity to the surroundings, make these TMD systems complex and different from traditional optical systems. Thus, characterizing their optical properties and understanding the underlying dynamics are important and necessary for their fundamental studies and optoelectronic and optical applications such as in light-emitting devices,[30–33] phototransistors,[34] and solar cells.[35]

As is well-known, radiated luminescence results from the recombination of the populating excited states of carriers.[36–43] Thus, recently, significant effort has been made to explore the dynamic processes of carrier interaction to understand the details of luminescence in the TMD systems, including interactions among carriers, carrier-scattering processes, and the mechanism for exciton recombination. Different interpretations were provided due to the complexity and variety of samples obtained from different synthetic methods. Herein, we systematically studied the exciton-recombination dynamics of monolayer WS_2 *via* a combination of results obtained from Raman, PL, and time-resolved PL spectroscopies at various excitation powers and different temperatures on the chemical vapor deposition (CVD)-grown samples. We attributed the two

[a]*Key Laboratory for Micro-Nano Physics and Technology of Hunan Province, School of Physics and Electronic Science, and State Key Laboratory of Chemo/Biosensing and Chemometrics, Hunan University, Changsha, Hunan 410082, P. R. China. E-mail: hongjun_l@outlook.com, anlian.pan@hnu.edu.cn*

[b]*Department of Chemistry and Biochemistry and California Nano Systems Institute, University of California at Los Angeles, Los Angeles, California 90095, USA*

†Electronic supplementary information (ESI) available. See DOI: 10.1039/c7nr01345k

‡These authors contributed equally to this work.

components in the PL transient dynamics to the decay time constants for trions and excitons. Then, based on carrier interaction, we interpreted the nonlinear changes, such as a red-shift and parabolic increase in the PL intensity, in the photoluminescence. Our results provide important information for the development of optoelectronic and optical application of TMDs materials: for example, for designing and constructing light-emitting diode (LED) devices and photodetectors.

Experimental

Synthesis

Samples for optical measurements were grown on SiO_2/Si substrates *via* CVD methods, with the charge materials being high purity WS_2 powder (99.99% purity, Alfa Aesar). Prior to thermal deposition, a SiO_2/Si wafer was diced into 1 × 1 cm^2 pieces and washed in an ultrasonic bath with acetone and isopropanol. Subsequently, the substrates were transferred into a quartz tube reactor (diameter 25 mm). During the evaporation of the WS_2 powder, the substrates were kept at 850 °C for 10 min under an argon flow of about 80 sccm under atmospheric pressure.

Characterization

Raman and photoluminescence measurements on the as-grown monolayer WS_2 were performed using a confocal microscope (WITec, alpha-300) with a CW 532 nm laser. PL spectra at room temperature were obtained using a 100× objective lens, whereas variable-temperature PL measurements were performed using a 20× objective lens with a commercially available liquid N_2 cooled stage. During our experiments, the laser beam was focused on a ~0.5 or 1 μm diameter spot. The incident laser power was calibrated using a power meter (PM100D from THORLABS) before each measurement. Time-resolved PL measurements were performed *via* a streak camera (C10910, Hamamatsu) using laser pulses at 400 nm (repetition rate of 80 MHz, pulse width of 80 fs) as the light source. The 400 nm output was generated by an 800 nm laser from a mode-locked oscillator (Tsunami 3941-X1BB, Spectra-Physics) placed after a BBO crystal. The laser beam was focused onto the sample on a quartz substrate using an objective lens (20×, Zeiss, 0.4NA), and PL emissions were obtained *via* the same objective lens. The time resolution of this system was 2.6 ps.

Results and discussion

WS_2 nanosheets with a size of tens of μm were grown *via* the CVD method, as shown in the optical image in Fig. 1a. The line profile of the atomic force microscopy (AFM) image indicates that the as-grown sample is a monolayer with a thickness of 0.7 nm. The single sharp peak in the PL spectrum was located at 636 nm, and the out-of-plane (A_{1g}) and in-plane Raman modes were located at ~351.9 cm^{-1} and ~417.2 cm^{-1}, respectively (refer to the ESI, Fig. S1†), which agrees well with the previous optical characterization of monolayer WS_2.[7] The

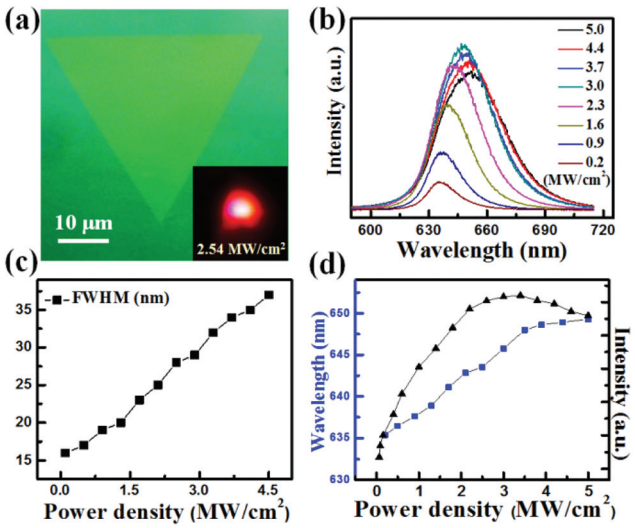

Fig. 1 Optical characterization of a CVD-grown monolayer WS_2. (a) An optical image of the as-grown sample. The inset shows the far dark-field optical image with strong red light emission observed in the monolayer WS_2 under a 532 nm laser with an excitation energy of 2.54 MW cm^{-2}. (b) PL spectra of the monolayer WS_2 under different excitation powers, and the corresponding FWHM of the PL spectra is plotted in the inset of (c). (d) Plots of the PL spectra intensity and peak position of the monolayer WS_2 under various excitation powers. The system error for the PL measurements is 0.2 cm^{-1}.

strong red light emission in this monolayer WS_2, shown in the far dark-field optical image in the inset of Fig. 1a, indicates the high quality of the CVD-grown sample. A series of PL measurements were performed on the as-grown WS_2 monolayers at room temperature to study their excitation power-dependence of PL, and the selected results are shown in Fig. 1b. Note that the full width at half maximum (FWHM), the emission intensity, and the peak positions of the PL spectra dramatically changed when the excitation power increased, as shown in Fig. 1c and d.

At a lower excitation power, such as 0.2 MW cm^{-2}, the peak position of the emission band was located at 636 nm, which was related to the bandgap emission of the monolayer WS_2 (1.95 eV) at room temperature. As the excitation power increases, the emission peak positions show a continuous red-shift during the experiments (Fig. 1d). Moreover, the emission intensities rapidly increased and quickly reached the saturation intensity at a high excitation power of 3 MW cm^{-2} and even exhibited a slower decrease with the further increase in power (Fig. 1d). The abovementioned experiments are fully reversible (refer to the ESI, Fig. S2†) and hence the degradation of the samples because of the strong excitation laser can be excluded. The Gaussian shape of the obtained PL spectra, different from that of the chopped PL spectrum with a longer integration time at a high excitation power density, also indicated that PL intensity saturation with the increasing excitation power was real and did not originate from the limitation of the confocal microscopy system (refer to the ESI S3†). Moreover, the measurement results were found to be

independent of the acquired positions and sizes of the obtained samples in our experiments.

Usually, laser radiation increases the carrier density of a sample and possibly heats the sample, both of which cause a red-shift in the PL.[28,44] Raman spectra in Fig. 2a show the invariableness of the in-plane mode E_{2g} and a linear decrease of the out-of-plane A_{1g} mode as the excitation power increases. From previous reports, it was observed that the E_{2g} mode was sensitive to temperature and shifted to a lower frequency when the sample was heated over a temperature range from 77 to 623 K for both the monolayer and multilayer WS_2.[45,46] In our experiments, no change in the peak position of the E_{2g} mode with the increase in the excitation power indicates that the in-plane lattice of the sample does not change during laser irradiation, as shown in Fig. 2b, which rules out the heating effect from the laser during our experiments. Therefore, the red-shift in the peak position and the parabolic increase in the emission intensity should be attributed to the increase in the carrier density caused by the laser radiation rather than to the thermal effect from the laser, agreeing with the reported theoretical work on MoS_2 by Gies *et al.*[44] For the pristine monolayer WS_2, the conduction band minimum was located at the K point, as shown in Fig. 2c. With the increasing excitation power, the energy at Λ point lowered faster than that at K point, leading to a shift in the conduction band minimum from K point to Λ point, as schematically shown in Fig. 2d. Carrier drain effects may lead to a parabolic increase in the PL intensities.

We also studied the excitation power dependence of the PL wavelengths and intensity of the monolayer WS_2 at various temperatures: 80 K, 200 K, 320 K, and 440 K; the results are plotted in Fig. 3 (refer to the ESI Fig. S4† for the spectra). Similar results as the above experiments at room temperature were collected. At each temperature, the PL intensity increased with the increasing excitation power and some PL emissions reached the saturation intensity at some excitation powers (Fig. 3b), whereas the PL emission peak showed a continuous red-shift under the same conditions (Fig. 3c). Due to the limitation of the laser power density of the variable-temperature confocal system used for these experiments, a decrease in the PL emissions was not obtained.

Time-resolved PL was performed on a monolayer WS_2 nanosheet to understand the abovementioned nonlinear changes obtained from the PL measurements. Fig. 4a is a

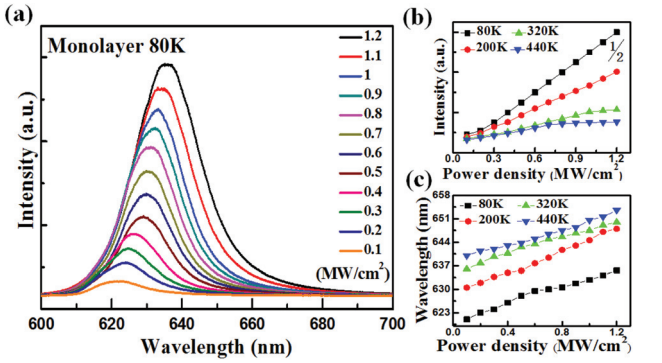

Fig. 3 Optical characterization of the monolayer WS_2 at different excitation powers and various temperatures. (a) The selected PL spectra of the monolayer WS_2 nanosheet at different excitation powers obtained at 80 K. The corresponding PL spectra intensity and peak position are plotted in (b) and (c), respectively, including more measurements carried out at 200 K, 320 K, and 440 K.

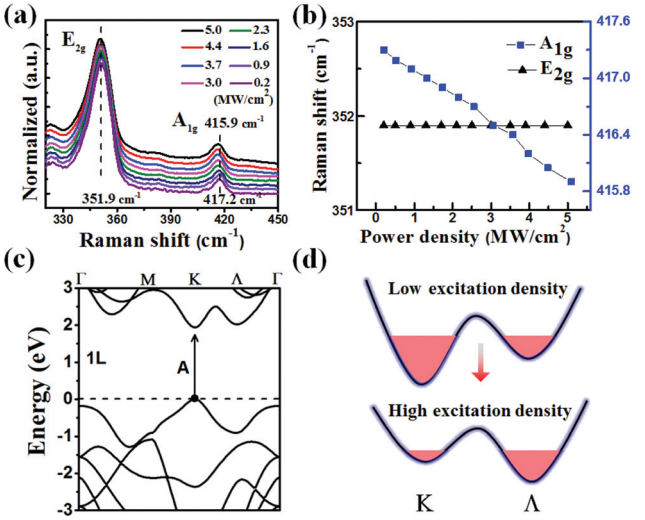

Fig. 2 Raman characterization and band structure of the monolayer WS_2. (a) Raman spectra of the monolayer WS_2 obtained at different excitation powers. (b) A_{1g} and E_{2g} Raman modes of the monolayer WS_2 obtained at various excitation powers. (c) Band structure of the pristine monolayer WS_2. (d) Schematic of the band structure renormalization of the monolayer WS_2 as the carrier density increases, based on a previous report.[44] The system error for Raman measurements is 0.2 cm^{-1}.

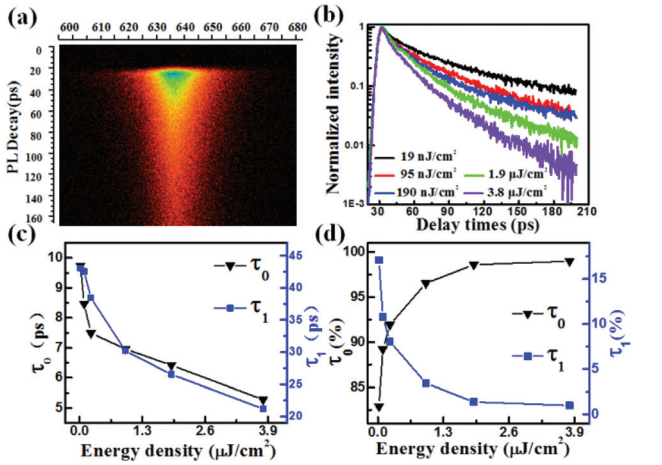

Fig. 4 Transient dynamic of the monolayer WS_2 at 300 K. (a) Selected streak camera image of the CVD-grown monolayer WS_2 obtained at 19 nJ cm^{-2} and 300 K. (b) Excitation dynamics at different excitation fluences with a time scale of 200 ps. These data are normalized by the maximum intensity for comparison. (c) Biexponentially fitted carrier decay time constants from the time-resolved spectra in (b), which clearly consist of two components, τ_0 and τ_1. The weight percent of these two components in the total decay rate constants are listed in (d).

selected streak camera image of the PL measurement at 300 K, and Fig. 4b shows the time-resolved PL spectra obtained from the streak camera images at different excitation fluences. These data were analyzed with single and biexponential decay fit (refer to the ESI, Fig. S5†), and it was found that biexponential decay could fit these data better. The obtained decay time constants from the biexponential fit are shown in Fig. 4c, which clearly consists of two components: a faster decay time constant τ_0 of several ps and a slower decay time constant τ_1 of tens of ps. Both decay time constants decrease with the increasing excitation fluences. Fig. 4d shows the change in the weights of τ_0 and τ_1 with the increasing excitation fluences. As the excitation fluences increase, the weight of τ_0 increases and even reaches nearly 100% at a power of 3.8 μJ cm^{-2}, whereas that of τ_1 sharply decreases, almost to nearly 0.

To understand the nature of these two components with different decay time constants in the abovementioned experiments, time-resolved PL spectra measurements were also performed at various temperatures, and the corresponding decay profiles are shown in Fig. 5a. The biexponential decay fit results obtained from the above mentioned profiles are presented in Fig. 5b and c, all of which also show two components with different time constants. These two decay time constants, τ_0 and τ_1, increase with the increasing temperatures, and the corresponding weight changes at the same time.

Moreover, two components with different decay time constants have also been reported in other TMDs and different explanations were proposed.[41,43,47–50] The long and short components were suggested to be the radiation decay time of trions and excitons, respectively, in Wang's work.[47] However, in Yan's report,[50] a contrary conclusion was drawn. The difference between these two conclusions[47,50] was attributed to the interaction between the carriers and the defects, which was commonly observed for the excitons in GaAs quantum well states.[51,52] Usually, CVD-grown TMDs have more defects than mechanically foliated samples, leading to a inferior optical performance.[53] For our CVD-grown samples, the peak positions for the radiation of trions and excitons cannot be distinguished because of the strong interaction between the carriers and defects even at 78 K. These defects may play a role during the radiation of the excitons and trions, which cannot be completely excluded in our experiments. The beam size, about 1 μm in our experiments, is much larger than that of the defects; thus, no individual defect effect can be identified. However, no peak for the bound excitons, as reported by Tongay,[54] was observed in the PL spectra in our experiments. Therefore, we suggested that the decay time constants τ_0 and τ_1 correspond to the recombination of trions and excitons, respectively, as reported in previous studies.[50] Due to the spatial confinement and reduced dielectric screening, excited electrons in the conduction band minimum (CBM) can have a strong Coulomb interaction with the holes in the valence band maximum (VBM) and form excitons with giant exciton binding energies in the 2D TMD system,[17–21] schematically shown in Fig. 6a. When an additional excited electron or hole joins the exciton, trions will be formed.[28,55] The schematic models of excitons and trions are shown in Fig. 6b. With the increasing excitation fluences, the excited carrier density increases, along with increase in excited electrons, holes, and excitons. The interaction among the excitons and electrons (holes) forces electrons (holes) into excitons to form the trions, providing a larger ratio of trions (Fig. 4d), as reported by Currie *et al.*[56] Moreover, the increasing carrier density leads to a stronger interaction and heavier scattering among different carriers,

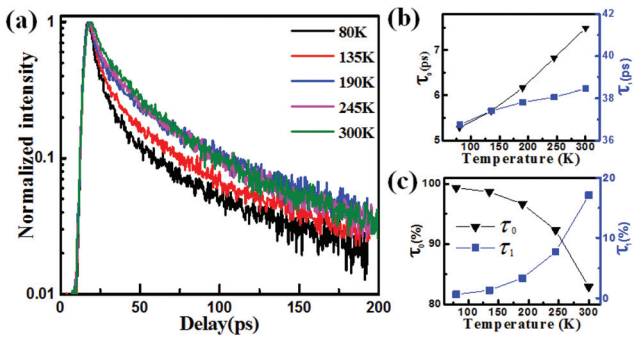

Fig. 5 Transient dynamics of the monolayer WS_2 at different temperatures. (a) Excitation dynamics at various temperatures and at 19 nJ cm^{-2} with a time scale of 200 ps. These data are normalized by the maximum intensity for comparison. (b) The decay time constants (τ_0 and τ_1) obtained from the biexponentially fitted PL decays in (a). (c) The weight percentages of these two components.

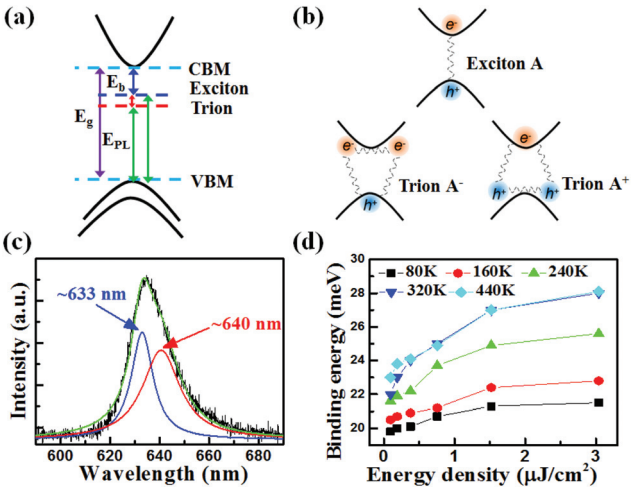

Fig. 6 Binding energies of the trions in the monolayer WS_2 at different energy densities. (a and b) The schematic for the energy level and the model of exciton and trion in 2D TMDs. Due to spatial confinement and reduced dielectric screening, an obvious exciton energy level occurs below the conduction band minimum. When an additional electron (hole) joins the exciton, a trion energy level occurs just below the exciton level. (c) A PL spectra of the monolayer WS_2 extracted from the streak camera image at 300 K, which is fitted with two Lorentzian peaks. The fit results clearly show that the obtained PL peak consists of two components, with a wavelength of 633 nm and 640 nm. These two peaks are attributed to the PL spectra for excitons and trions, and the energy difference between these two peaks at different excitation energies and different temperatures are presented in (d).

which increases the probabilities for the relaxation of both the trions and excitons and thus results in faster decay times, as shown in Fig. 4c. Note that both τ_0 and τ_1 were reduced to half when the excitation fluence increased from 19 nJ cm^{-2} to 3.8 μJ cm^{-2}, *i.e.*, the rate for the change of decay time constant was almost the same. Thus, the carrier interaction and scattering seems to similarly affect the trions and excitons. For temperature-dependent experiments, as shown in Fig. 5b, our hypothesis also agrees well with the experimental data. The increase in the decay time constant with the increasing temperatures agrees with the reported theoretical work and experiments on the monolayer MoS_2.[40,57] Since the binding energy of trions is of tens of meV, trions will become unstable due to the increase in the thermal fluctuation energy as the temperature increases, leading to a smaller ratio, as shown in Fig. 5c. For the recombination of excitons and trions, the increase in diffusion with the increasing temperatures will make the decay time constant longer,[57] which agrees well with the trend shown in Fig. 5b.

Furthermore, the binding energies for trions under various conditions were studied. Herein, the binding energy of trions is defined as the energy difference between the excitons and trions. Fig. 6c shows the PL spectrum extracted from the streak camera image shown in Fig. 4a, which appears asymmetric because the right baseline is higher than the left baseline. This PL spectrum was fitted to two Lorentzian peaks with the peak wavelengths of 633 nm and 640 nm, shown as blue and red curves in Fig. 6c. Thus, the binding energy for this trion is about 21 meV, agreeing with the reported binding energies for TMDs.[21,28] More binding energies for the trions under various excitation fluences and at different temperatures are plotted in Fig. 6d. With the increasing temperatures, the binding energies also increased, agreeing with the variable-temperature experimental results reported by Xu *et al.*[28] For the binding energies at 320 K and 400 K, almost no difference was observed. On the other hand, as the excitation fluence increases, the increasing carrier density can stabilize the trions, leading to an increase in the binding energies. The calculated binding energies further confirmed our abovementioned hypothesis.

The carrier interaction observed from the time-resolved PL can provide a good interpretation of the parabolic increase in the red-shift and PL intensity with the increasing excitation fluences. As the excitation fluence increases, the ratio of trions becomes larger and larger, leading to a red-shift in the PL. Moreover, the decay time constant for the recombination of excitons and trions becomes shorter, *i.e.*, the rate for the recombination of trions and excitons is enhanced, which provides a stronger radiation. Fig. 4c shows that the rate for the decrease in the decay time constant becomes slower with the increasing excitation fluences. When the excitation fluence is sufficiently high, the decay time constant does not decrease further, and the PL emission reaches saturation emission. At this excitation fluence, other interactions, such as non-radiation recombination and exciton–phonon interaction, among carriers will also play important roles and lead to a decrease in the PL intensity. In addition, the stronger interaction caused by the increasing carrier density weakens the bonding between the W atoms and S atoms, leading to a decrease in the vibrational frequency of the Raman out-of plane A_{1g} mode, as shown in Fig. 2b.[58] Moreover, the increasing interaction and scattering of the density-increasing carriers will broaden the radiated PL, leading to an increase in the FWHM (Fig. 1c). For temperature-dependent experiments, the higher PL intensity at lower temperature can also be attributed to the decreasing decay time constant with the decreasing temperature. Since the intrinsic concentration of the carrier is much lower at lower temperature, the PL intensity increases much faster than that at higher temperature with the increasing excitation fluences. For example, the rate for the PL intensity increase at 80 K is much higher than that at 400 K.

Herein, the theoretical explanation of the red-shift and the parabolic intensity increase in the PL spectra, as shown in Fig. 2d, has been provided. We speculated that this type of band structure renormalization should also contribute to the red-shift and parabolic intensity increase, especially for the PL spectra under high excitation fluences, such as at a power density larger than 3 MW cm^{-2}. According to reports, as the carrier density increases, the position of the Λ valley in the conduction band is lowered faster than that of the K valley by multi-particle renormalizations, leading to the accumulation of electrons and non-radiative annihilation in the Λ valley, as schematically shown in Fig. 2d.[44] Carrier drain from the K valley to the Λ valley results in the quenching of PL, which originates from the radiative recombination of photoexcited carriers at the K valley. In our time-resolved experiments, the binding energy for trions was about 20–30 meV (7–10 nm in wavelength), as shown in Fig. 6d, while the red-shift of excitons was around 12 meV (4–5 nm in wavelength) with the increasing excitation fluence (refer to the ESI, Fig. S6†). The red-shift of excitons (12 mev) may be attributed to the band structure renormalization, during which the conduction band minimum at the K point is lowered with the increasing carrier density. The combination effects from the ratio change of trions and excitons and the red-shift of excitons may provide the total red-shift, as shown in Fig. 1b (14 nm in wavelength). On the other hand, the decreasing decay time constant cannot be used to interpret the small intensity decrease, as shown in Fig. 1d, which should be from carrier drain from the K valley to the Λ valley. The indirect transition from the conduction band minimum at the Λ valley to the valence band maximum at the K valley is an intervalley recombination process with the time constant at the ns scale.[42] However, our steak camera could not detect this type of indirect transition due to very low intensity of its luminescence.[21,59] In the streak camera image shown in Fig. 4a, no obvious brightness was observed at the wavelength of 670–680 nm, the wavelength for the indirect transition from the conduction band minimum at the Λ valley to the valence band maximum at the K valley. Therefore, we believe that both the carrier interaction and band structure renormalization contribute to the nonlinear change of PL emission.

Conclusions

In conclusion, the excitation fluence and temperature-dependent carrier interactions in the monolayer WS_2 were studied *via* a combination of PL, Raman, and time-resolved PL spectra. The two components τ_0 and τ_1 in the transient PL decays are attributed to the decay time constants for the recombination of trions and excitons, respectively. Both the carrier interaction and band structure renormalization are believed to contribute to the nonlinear changes, such as the red-shift and parabolic increase of the PL emission, in the PL spectra with the increasing excitation fluences. Furthermore, the temperature-dependent PL properties can also be explained well *via* the carrier interaction. The observation and understanding of the nonlinear PL will provide valuable information for future optoelectronic and optical measurements and device applications of atomic-layered semiconductors since the devices will be used under various surroundings and various excitation fluences. Furthermore, our findings on the CVD-grown WS_2 samples may also be applicable in other TMD materials since they have the same atomically thin sandwiched structures.

Contributions

All authors extensively contributed to the work presented in this study. HJL and ALP conceived the study, designed or co-designed all the experiments presented herein, and wrote the major part of the manuscript with the assistance of HLL, XPW, YJ, XLZ, HZ, WH and XFD. XPF, YFG, and WHZ prepared the sample and performed the measurements. PF, XJZ, XW and QLZ constructed the low-temperature experimental set-up.

Acknowledgements

The authors are grateful to the National Natural Science Foundation of China (no. 11374092, 51672076, 61474040, 61574054, 61505051), the Aid Program for Science and Technology Innovative Research Team in Higher Educational Institutions of Hunan Province, the Hunan Provincial Science and Technology Department (no. 2014FJ2001, 2014GK3015, 2014TT1004), and the Joint Research Fund for Overseas Chinese, Hong Kong and Macau Scholars of the National Natural Science Foundation of China (no. 61528403). The authors thank J. W. Liang at the Yulin Normal University for providing the electronic band calculation of the monolayer structure.

Notes and references

1 Q. H. Wang, K. Kalantar-Zadeh, A. Kis, J. N. Coleman and M. S. Strano, *Nat. Nanotechnol.*, 2012, **7**, 699–712.
2 K. F. Mak, C. Lee, J. Hone, J. Shan and T. F. Heinz, *Phys. Rev. Lett.*, 2010, **105**, 136805.
3 D. Xiao, G. BLiu, W. Feng, X. Xu and W. Yao, *Phys. Rev. Lett.*, 2012, **108**, 196802.
4 K. F. Mak, K. He, J. Shan and T. F. Heinz, *Nat. Nanotechnol.*, 2012, **7**, 494–498.
5 H. Zeng, J. Dai, W. Yao, D. Xiao and X. Cui, *Nat. Nanotechnol.*, 2012, **7**, 490–493.
6 T. Cao, G. Wang, W. P. Han, H. Q. Ye, C. R. Zhu, J. R. Shi, Q. Niu, P. H. Tan, E. Wang, B. L. Liu and J. Feng, *Nat. Commun.*, 2012, **3**, 177–180.
7 W. Zhao, Z. Ghorannevis, L. Chu, M. Toh, C. Kloc, P. H. Tan and G. Eda, *ACS Nano*, 2012, **7**, 791–797.
8 D. Ovchinnikov, A. Allain, Y. S. Huang, D. Dumcenco and A. Kis, *ACS Nano*, 2014, **8**, 8174–8181.
9 S. Jo, N. Ubrig, H. Berger, A. B. Kuzmenko and A. F. Morpurgo, *Nano Lett.*, 2014, **14**, 2019–2025.
10 X. Duan, C. Wang, J. C. Shaw, R. Cheng, Y. Chen, H. Li, X. Wu, Y. Tang, Q. Zhang, A. Pan, J. Jiang, R. Yu, Y. Huang and X. Duan, *Nat. Nanotechnol.*, 2014, **9**, 1024–1030.
11 C. Ge, H. Li, X. Zhu and A. Pan, *Chin. Phys. B*, 2017, **26**, 034208.
12 H. Li, X. Duan, X. Wu, X. Zhuang, H. Zhou, Q. Zhang, X. Zhu, W. Hu, P. Ren, P. Guo, L. Ma, X. Fan, X. Wang, J. Xu, A. Pan and X. Duan, *J. Am. Chem. Soc.*, 2014, **136**, 3756–3759.
13 H. Li, Q. Zhang, X. Duan, X. Wu, X. Fan, X. Zhu, X. Zhuang, W. Hu, H. Zhou, A. Pan and X. Duan, *J. Am. Chem. Soc.*, 2015, **137**, 5284–5287.
14 X. Duan, C. Wang, A. Pan, R. Yu and X. Duan, *Chem. Soc. Rev.*, 2016, **47**, 81–87.
15 X. Duan, C. Wang, Z. Fan, G. Hao, L. Kou, U. Halim, H. Li, X. Wu, Y. Wang, J. Jiang, A. Pan, Y. Huang, R. Yu and X. Duan, *Nano Lett.*, 2016, **16**, 264–269.
16 H. Li, X. Wu, H. Liu, B. Zheng, Q. Zhang, X. Zhu, Z. Wei, X. Zhuang, H. Zhou, W. Tang, X. Duan and A. Pan, *ACS Nano*, 2017, **11**, 961–967.
17 K. He, N. Kumar, L. Zhao, Z. Wang, K. F. Mak, H. Zhao and J. Shan, *Phys. Rev. Lett.*, 2014, **113**, 026803.
18 Z. Ye, T. Cao, K. O. Brien, H. Zhu, X. Yin, Y. Wang, S. G. Louie and X. Zhang, *Nature*, 2014, **513**, 214–218.
19 D. Y. Qiu, F. H. da Jornada and S. G. Louie, *Phys. Rev. Lett.*, 2013, **111**, 216805.
20 B. Zhu, X. Chen and X. Cui, *Sci. Rep.*, 2015, **5**, 9218.
21 H. J. Liu, L. Jiao, L. Xie, F. Yang, J. L. Chen, W. K. Ho, C. L. Gao, J. F. Jia, X. D. Cui and M. H. Xie, *2D Mater.*, 2015, **2**, 034004.
22 K. F. Mak, K. He, C. Lee, G. H. Lee, J. Hone, T. F. Heinz and J. Shan, *Nat. Mater.*, 2012, **12**, 207–211.
23 G.-B. Liu, D. Xiao, Y. Yao, X. Xu and W. Yao, *Chem. Soc. Rev.*, 2014, **44**, 2643–2663.
24 H. R. Gutiérrez, N. Perea-López, A. L. Elías, A. Berkdemir, B. Wang, R. Lv, F. López-Urías, V. H. Crespi, H. Terrones and M. Terrones, *Nano Lett.*, 2013, **13**, 3447–3454.
25 A. M. van der Zande, P. Y. Huang, D. A. Chenet, T. C. Berkelbach, Y. You, G.-H. Lee, T. F. Heinz, D. R. Reichman, D. A. Muller and J. C. Hone, *Nat. Mater.*, 2013, **12**, 554–561.

26 H. Nan, Z. Wang, W. Wang, Z. Liang, Y. Lu, Q. Chen, D. He, P. Tan, F. Miao, X. Wang, J. Wang and Z. Ni, *ACS Nano*, 2014, **8**, 5738–5745.
27 S. Tongay, J. Suh, C. Ataca, W. Fan, A. Luce, J. S. Kang, J. Liu, C. Ko, R. Raghunathanan, J. Zhou, F. Ogletree, J. Li, J. C. Grossman and J. Wu, *Sci. Rep.*, 2013, **3**, 2657.
28 J. S. Ross, S. Wu, H. Yu, N. J. Ghimire, A. M. Jones, G. Aivazian, J. Yan, D. G. Mandrus, D. Xiao, W. Yao and X. Xu, *Nat. Commun.*, 2013, **4**, 1474.
29 S. Tongay, J. Zhou, C. Ataca, K. Lo, T. S. Matthews, J. Li, J. C. Grossman and J. Wu, *Nano Lett.*, 2012, **12**, 5576–5580.
30 J. S. Ross, P. Klement, A. M. Jones, N. J. Ghimire, J. Yan, D. G. Mandrus, T. Taniguchi, K. Watanabe, K. Kitamura, W. Yao, D. H. Cobden and X. Xu, *Nat. Nanotechnol.*, 2014, **9**, 268–272.
31 C. Chakraborty, L. Kinnischtzke, K. M. Goodfellow, R. Beams and A. N. Vamivakas, *Nat. Nanotechnol.*, 2015, **10**, 507–511.
32 X. Wang, X. Zhuang, S. Yang, Y. Chen, Q. Zhang, X. Zhu, H. Zhou, P. Guo, J. Liang, Y. Huang, A. Pan and X. Duan, *Phys. Rev. Lett.*, 2015, **115**, 027403.
33 S. Wu, S. Buckley, J. R. Schaibley, L. Feng, J. Yan, D. G. Mandrus, F. Hatami, W. Yao, J. Vuckovic, A. Majumdar and X. Xu, *Nature*, 2015, **520**, 69–72.
34 H. Li, J. Wu, X. Huang and H. Zhang, *ACS Nano*, 2013, **7**, 10344–10353.
35 A. Pospischil, M. M. Furchi and T. Mueller, *Nat. Nanotechnol.*, 2014, **9**, 257–261.
36 X. Marie and B. Urbaszek, *Nat. Mater.*, 2015, **14**, 860–861.
37 D. Lagarde, L. Bouet, X. Marie, C. R. Zhu, B. L. Liu, T. Amand, P. H. Tan and B. Urbaszek, *Phys. Rev. Lett.*, 2014, **112**, 047401.
38 H. M. Hill, A. F. Rigosi, C. Roquelet, A. Chernikov, T. C. Berkelbach, D. R. Reichman, M. S. Hybertsen, L. E. Brus and T. F. Heinz, *Nano Lett.*, 2015, **15**, 2992–2997.
39 A. Chernikov, C. Ruppert, H. M. Hill, A. F. Rigosi and T. F. Heinz, *Nat. Photon.*, 2015, **9**, 466–470.
40 D. Sun, Y. Rao, G. A. Reider, G. Chen, Y. You, L. Brézin, A. R. Harutyunyan and T. F. Heinz, *Nano Lett.*, 2014, **14**, 5625–5629.
41 S. Sim, J. Park, J.-G. Song, C. In, Y.-S. Lee, H. Kim and H. Choi, *Phys. Rev. B: Condens. Matter*, 2013, **88**, 075434.
42 H. Shi, R. Yan, S. Bertolazzi, J. Brivio, B. Gao, A. Kis, D. Jena, H. G. Xing and L. Huang, *ACS Nano*, 2013, **7**, 1072–1080.
43 C. Mai, A. Barrette, Y. Yu, Y. G. Semenov, K. W. Kim, L. Cao and K. Gundogdu, *Nano Lett.*, 2014, **14**, 202–206.
44 A. Steinhoff, J. H. Kim, F. Jahnke, M. Rösner, D. S. Kim, C. Lee, G. H. Han, M. S. Jeong, T. O. Wehling and C. Gies, *Nano Lett.*, 2015, **15**, 6841–6847.
45 M. Thripuranthaka and D. J. Late, *ACS Appl. Mater. Interfaces*, 2014, **6**, 1158–1163.
46 M. Thripuranthaka, R. V. Kashid, C. Sekhar Rout and D. J. Late, *Appl. Phys. Lett.*, 2014, **104**, 081911–081915.
47 G. Wang, L. Bouet and D. Lagarde, *Phys. Rev. B: Condens. Matter*, 2014, **90**, 075413.
48 L. Yuan and L. Huang, *Nanoscale*, 2015, **7**, 7402–7408.
49 S. Mouri, Y. Miyauchi, M. Toh, W. Zhao, G. Eda and K. Matsuda, *Phys. Rev. B: Condens. Matter*, 2014, **90**, 155449.
50 T. Yan, X. Qiao, X. Liu, P. Tan and X. Zhang, *Appl. Phys. Lett.*, 2014, **105**, 101901–101904.
51 D. Sanvitto, R. A. Hogg, A. J. Shields, D. M. Whittaker, M. Y. Simmons and D. A. Ritchie, *Phys. Rev. B: Condens. Matter*, 2000, **62**, 13294.
52 G. Finkelstein, I. Bar-Joseph, V. Ciulin, S. Haacke and B. Deveaud, *Phys. Rev. B: Condens. Matter*, 1998, **58**, 12637.
53 W. Zhao, Z. Ghorannevis, L. Chu, M. Toh, C. Kloc and P. H. Tan, *ACS Nano*, 2013, **7**, 791–797.
54 S. Tongay, J. Suh, C. Ataca, W. Fan, A. Luce and J. S. Kang, *Sci. Rep.*, 2013, **3**, 2657.
55 A. Boulebaa, B. Huang, K. Wang, M. W. Lin, M. M. Samani, C. Rouleau, K. Xiao, M. Yoon, B. Sumpter, A. Puuretzky and D. Geohegan, *Phys. Rev. B: Condens. Matter*, 2015, **92**, 115443.
56 M. Currie, A. T. Hanbicki, G. Kioseoglou and B. T. Jonker, *Appl. Phys. Lett.*, 2015, **106**, 201907–201905.
57 H. Wang, C. Zhang, W. Chan, C. Manolatou, S. Tiwari and F. Rana, *Phys. Rev. B: Condens. Matter*, 2016, **93**, 045407.
58 B. Chakraborty, A. Bera, D. V. S. Muthu, S. Bhowmick, U. V. Waghmare and A. K. Sood, *Phys. Rev. B: Condens. Matter*, 2012, **85**, 161403.
59 H. Zeng, G.-B. Liu, J. Dai, Y. Yan, B. Zhu, R. He, L. Xie, S. Xu, X. Chen, W. Yao and X. Cui, *Sci. Rep.*, 2013, **3**, 1608.